Journal of Materials Chemistry A

ROYAL SOCIETY OF CHEMISTRY

PAPER

View Article Online
View Journal | View Issue

Cite this: J. Mater. Chem. A, 2020, 8, 18079

Origin of the extra capacity in nitrogen-doped porous carbon nanofibers for high-performance potassium ion batteries†

Fang Liu,[ab] Jiashen Meng,[a] Fanjie Xia,[ab] Ziang Liu,[a] Haoyang Peng,[ab] Congli Sun,[ab] Linhan Xu,[*de] Gustaf Van Tendeloo,[bc] Liqiang Mai[*a] and Jinsong Wu[*ab]

Received 5th June 2020
Accepted 2nd August 2020

DOI: 10.1039/d0ta05626j

rsc.li/materials-a

While graphite has limited capacity as an anode material for potassium-ion batteries, nitrogen-doped carbon materials are more promising as extra capacity can usually be produced. However, the mechanism behind the origin of the extra capacity remains largely unclear. Here, the potassium storage mechanisms have been systematically studied in freestanding and porous N-doped carbon nanofibers with an additional ~100 mA h g^{-1} discharge capacity at 0.1 A g^{-1}. The extra capacity is generated in the whole voltage window range from 0.01 to 2 V, which corresponds to both surface/interface K-ion absorptions due to the pyridinic N and pyrrolic N induced atomic vacancies and layer-by-layer intercalation due to the effects of graphitic N. As revealed by transmission electron microscopy, the N-doped samples have a clear and enhanced K-intercalation reaction. Theoretical calculations confirmed that the micropores with pyridinic N and pyrrolic N provide extra sites to form bonds with K, resulting in the extra capacity at high voltage. The chemical absorption of K-ions occurring inside the defective graphitic layer will prompt fast diffusion of K-ions and full realization of the intercalation capacity at low voltage. The approach of preparing N-doped carbon-based materials and the mechanism revealed by this work provide directions for the development of advanced materials for efficient energy storage.

Introduction

To meet the increasing energy demand, extensive efforts have been dedicated to exploring green and renewable electrochemical energy storage technologies, which could lead to the substitution of traditional non-renewable energy supplies (*e.g.* coal, oil, natural gases, *etc.*).[1–3] Rechargeable lithium-ion batteries (LIBs), as a dominating power source, have been considered as the most promising candidates for energy storage applications.[4,5] However, the mass production of LIBs is limited due to the low availability of lithium resources and the rising costs. Hence, other alkali metal ion (such as Na^+ and K^+) batteries have attracted attention due to the abundance of Na and K and their similar chemical properties to those of Li.[6,7] Compared to sodium-ion batteries (SIBs), potassium-ion batteries (PIBs) have a lower redox potential (−2.93 V for PIBs *vs.* −2.71 V for SIBs), which means that PIBs have a higher energy density than SIBs. Moreover, owing to their large ion radius, Na-ions cannot be directly intercalated into graphite which is essential for producing a commercializable anode. In contrast, K^+ ions can be intercalated into graphite to form potassium graphite intercalation compounds such as KC_8.[8] This is an advantage for mass production in the battery industry. Hence, research into graphitic carbons as anodes for PIBs has recently been promoted. However, even KC_8 in a fully intercalated state has a theoretical capacity of only 279 mA h g^{-1}, and the low capacity is one of the obstacles facing the development of PIBs. Moreover, the theoretical capacity is practically hard to realize.[9]

Particularly in the past decade, carbon-based materials have attracted extensive attention in energy storage because of their abundant sources, low cost, easy production and excellent chemical stability.[10–12] Recently, some efficient approaches have been further developed to endow novel carbon-based materials with high surface area and fast mass transport. One typical strategy is to design and construct nanostructured carbon materials to enhance the electrochemical performance for

[a]State Key Laboratory of Advanced Technology for Materials Synthesis and Processing, International School of Materials Science and Engineering, Wuhan University of Technology, Luoshi Road 122, Wuhan, 430070, Hubei, China. E-mail: mlq518@whut.edu.cn; wujs@whut.edu.cn

[b]NRC (Nanostructure Research Centre), Wuhan University of Technology, Wuhan 430070, China

[c]EMAT (Electron Microscopy for Materials Science), University of Antwerp, Belgium

[d]Department of Physics, Collaborative Innovation Center for Optoelectronic Semiconductors and Efficient Devices, Jiujiang Research Institute, Xiamen University, Xiamen, China. E-mail: intocadilian@126.com

[e]Department of Physics and Astronomy, Ames Laboratory of DOE, Iowa State University, Ames, IA 50011, USA

† Electronic supplementary information (ESI) available: X-ray diffraction, cyclic voltammetry, thermogravimetric analysis, morphology characterization, and electrochemical impedance spectroscopy. See DOI: 10.1039/d0ta05626j

PIBs.[13–15] For example, Wang *et al.* reported short-range order in mesoporous carbon, with a large interlayer spacing, a unique layered structure and high specific surface area, and thus a relatively high capacity as a PIB anode of about 257.4 mA h g^{-1} at a current density of 0.05 A g^{-1}.[16] Recently, Cao *et al.* reported a highly graphitic carbon nanocage with a 3D electrically conducting network and highly graphitic structure. This architecture allows for a fast electron transfer and ensures a low energy and stable K^+ intercalation/deintercalation, resulting in an excellent rate capability and good cycling stability for PIBs.[17] Another important strategy is the introduction of heteroatoms (*e.g.* nitrogen, sulfur, phosphorus, *etc.*) into the carbon lattice framework, which can efficiently alter their electronic structure and thereby result in high activity for energy conversion and storage.[18–21] Among these heteroatoms, nitrogen can be incorporated into the carbon framework and form strong interactions with active molecules/ions in the electrolyte due to their small size and high electronegativity.[22] Share *et al.* reported nitrogen doping of few-layered graphene as an anode material for PIBs with a storage capacity of 350 mA h g^{-1}, higher than that of graphite (278 mA h g^{-1}).[23] Xu *et al.* developed nitrogen-doped carbon nanofibers with a nitrogen content of ~13.8 wt%, exhibiting a high potassium storage capacity of 248 mA h g^{-1} at 25 mA g^{-1}.[24] These superior properties are mainly attributed to effects induced by the doped nitrogen. However, the detailed mechanism of nitrogen doping as the origin of this extra capacity, the electronic structure of carbon and the active/storage sites in these nitrogen-doped carbon materials still remain ambiguous due to the complexity of the nitrogen species. In this work, we tackle the mechanism by applying recent developments in both *ex situ* and *in situ* characterization methods to monitor the dynamic structural evolution during the electrochemical reactions.

In addition, fabrication of freestanding and flexible nitrogen-doped carbon electrodes is highly desired in order to decrease the inactive and/or low efficiency components in energy storage devices.[25–27] In this regard, the development of freestanding carbon-based nanostructures without additional materials as substrates is essential to achieve cost-effective and high-performance PIBs.[28] We report a facile and controllable method to fabricate freestanding, porous and nitrogen-doped carbon nanofibers (NCNFs) by electrospinning with confinement formation of nanocrystal templates and subsequent carbonization. By modulating the amount of nanocrystal templates and heat treatment temperature, the porosity and chemical composition of the obtained NCNF samples can be easily controlled. The as-prepared sample annealed at 800 °C possesses a high surface area, abundant pores and high nitrogen content, and exhibits remarkable potassium storage performance. While the freestanding NCNFs enable the full use of the materials as PIB electrodes, their mechanical flexibility has great potential for application in flexible energy devices (*i.e.* bendable batteries). Moreover, their cycling stability is confirmed by monitoring the volumetric evolution during potassiation using *in situ* transmission electron microscopy (TEM). The role of doped nitrogen is studied by *ex situ* electron energy loss spectroscopy (EELS) and density functional theory (DFT) calculations. All this provides further insight into the design of functional nitrogen-doped carbon materials for energy storage.

Experimental section

Synthesis of freestanding porous N-doped carbon nanofibers

0.4 g of $ZnNO_3 \cdot 6H_2O$, 1.6 g of $Zn(C_5H_7O_2)_2$, 2.0 g of 2-methylimidazole and 1.8 g of polyacrylonitrile were added in 22 mL of *N*,*N*-dimethylformamide solution. After stirring at room temperature for 3 h, the obtained viscous and white precursor solution was electrospun at a high voltage of 10 kV and −2 kV (electrospinning equipment: SS-2534H from UCALERY Co., Beijing, China). Finally, after the composite nanowires were pre-sintered at 220 °C (3 °C min^{-1}) in air for 1 h and annealed at 800 °C (5 °C min^{-1}) under an argon atmosphere for 3 h, uniform porous N-doped carbon nanofibers were obtained (NCNF-800). In comparison, when the composite nanowires were pre-sintered at 220 °C (3 °C min^{-1}) in air for 1 h and then treated at 1000 °C under an argon atmosphere for 3 h, the NCNF-1000 sample was obtained.

Characterization

The crystallographic characteristics of the final products were measured using a Bruker D8 Discover X-ray diffractometer equipped with a Cu Kα radiation source. SEM images were collected using a JEOL-7100F scanning electron microscope, and TEM images were collected using a JEM-2100F/Titan G2 60-300 transmission electron microscope. STEM-EELS spectra and images were recorded at 300 kV using a Titan microscope equipped with a Gatan image filter (GIF) spectrometer. Energy-dispersive X-ray spectra were recorded using an Oxford IE250 system. *In situ* TEM was performed by a TEM-STM *in situ* sample holder (ZepTools Co. Ltd., China). Raman spectra were obtained using a Renishaw inVia micro-Raman spectroscopy system. The BET surface area was calculated from nitrogen adsorption isotherms collected at 77 K using a Tristar-3020 instrument. XPS and UPS measurements were conducted using an ESCALAB 250Xi instrument.

Computational details

All simulations are based on density functional theory (DFT) and carried out by using the projector augmented wave (PAW) method as implemented in the Vienna *ab initio* simulation package (VASP). The exchange and correlation functional was treated as the generalized gradient approximation (GGA) of the Perdew–Burke–Ernzerhof (PBE) formula. The wave functions were expanded by using the plane waves up to a kinetic energy cutoff of 500 eV. Brillouin-zone integrations were approximated by using special *k*-point sampling of the Monkhorst–Pack scheme with a *k*-point mesh resolution of $2\pi \times 0.03$ $Å^{-1}$. The unit cell lattice vectors (unit cell shape and size) and atomic coordinates were fully relaxed until the force on each atom was less than 0.02 eV $Å^{-1}$.

Potassium storage measurements

The electrode film of freestanding porous carbon nanofibers was uniformly cut into ~2 cm^2 round slices, weighing ~4 mg; the corresponding areal mass loading was 2 mg cm^{-2}. The thickness of the electrode is about 100 μm as measured by cross-sectional SEM (Fig. S8†). 2016 coin cells were assembled in a glovebox filled with pure argon gas. Potassium foil was used as the counter electrode and the separator was a Celgard 2400 microporous membrane. 1 M potassium hexafluorophosphate (KPF_6) solution in ethylene carbonate (EC)–dimethyl carbonate (DMC) (1 : 1 v/v) was used as the electrolyte. Galvanostatic charge–discharge measurements were performed using a multichannel battery testing system (LAND CT2001A). CVs and electrochemical impedance spectra were collected at room temperature using an Autolab potentiostat/galvanostat.

Results and discussion

Synthesis and characterization

The synthesis procedure of freestanding porous NCNFs is illustrated in Fig. S1.† First, the precursor solution was prepared by mixing Zn^{2+} sources, 2-methylimidazole (2-MIM) and polyacrylonitrile (PAN) in *N*,*N*-dimethylformamide (DMF). As 2-MIM hardly deprotonates in DMF at room temperature, a viscous homogeneous solution of zeolitic imidazolate framework (ZIF) crystals is formed in the mixture. Under a strong electrostatic tension force along with the volatilization of DMF, the homogeneous solution is electrospun to form uniform precursor@PAN nanofibers. Then the precursor@PAN nanofibers are heated at 80 °C (denoted as step I). The formation of small ZIF-8 nanocrystals by the coordination reaction between zinc ions and 2-MIM, as well as the crystallization of the residual 2-MIM, results in both the ZIF-8 and 2-MIM nanocrystals being confined into the PAN nanofibers (ZIF-8 & 2-MIM@PAN). X-ray diffraction (XRD) patterns of ZIF-8 & 2-MIM@PAN nanofibers show obvious diffraction peaks from both the ZIF-8 and 2-MIM, confirming the existence of these crystals in the nanofibers (Fig. S2a, ESI†). As shown by scanning electron microscopy (SEM) (Fig. S2b–d, ESI†), the composite nanofibers have a uniform fibrous morphology with a rough surface and an average diameter of about 500 nm. Furthermore, TEM images demonstrate the existence of nanocrystals (<50 nm in diameter) in the nanofibers (Fig. S2e and f, ESI†). The formed ZIF-8 and 2-MIM nanocrystals act as hard templates in the step II process, *i.e.* the *in situ* carbonization. When the as-prepared ZIF-8 & 2-MIM@PAN nanofibers are treated at high temperature (≥800 °C) in an argon atmosphere, the pyrolysis of confined ZIF-8 nanocrystals and the volatilization of confined 2-MIM nanocrystals, together with the carbonization of PAN, result in the formation of freestanding carbon nanofibers with lots of pores with various sizes. Since N is retained in the nanofibers when the temperature is appropriate, porous NCNFs are obtained. In brief, the synthesis process includes fabrication of precursor nanofibers by electrospinning, confinement formation of nanocrystal templates and *in situ* carbonization. By modulating the number of nanocrystal templates and the heat treatment temperature, the porosity and chemical composition in the formed NCNFs can be effectively controlled as discussed below.

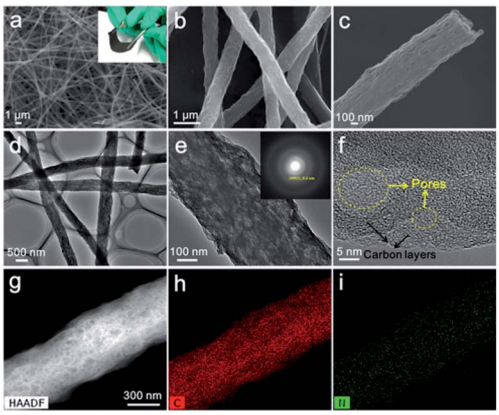

Fig. 1 Morphology characterization of porous NCNF-800. (a–c) SEM images. The inset of (a) is an optical image. (d and e) TEM images. The inset of (e) is a SAED pattern. (f) HRTEM image. (g–i) STEM-HAADF image and the corresponding STEM-EDS mapping images for C and N elements.

The morphology of the obtained NCNFs has been characterized by various techniques. When treated at 800 °C, the porous NCNFs (denoted as NCNF-800) show a uniform fibrous morphology with an average diameter of ~500 nm and they are assembled into a thin freestanding nanofiber film (Fig. 1a). The as-prepared films exhibit good flexibility and can directly act as a freestanding, binder-free and bendable electrode (inset of Fig. 1a). The enlarged SEM images clearly display the porous and wrinkled surface of NCNF-800 (Fig. 1b and c). TEM images (Fig. 1d and e) indicate that the nanofibers are porous, as there are many variations in image contrast. High-resolution TEM (HRTEM) (Fig. 1f and S4a, ESI†) shows that the graphitic layers are curved and defective, among which encapsulated pores with a size of 5–20 nm can be seen. The pores are mainly generated by the hard template removal during annealing. The selected-area electron diffraction (SAED) patterns of the NCNF-800 nanofibers (inset of Fig. 1e) show only a weak and diffuse diffraction ring, corresponding to an interplanar distance of about 0.4 nm, which is an indication of the presence of the expanded and defective (002) graphitic lattice planes and low graphitization of NCNF-800. STEM energy-dispersive X-ray spectroscopy (STEM-EDS) mapping (Fig. 1g–i) confirms that the N is uniformly distributed in the nanofibers. Samples that underwent a heat treatment at 1000 °C are denoted as NCNF-1000. The morphology of NCNF-1000 is similar to that of NCNF-800 as shown by the SEM images (Fig. S3, ESI†). However, with the increase of the treatment temperature, the surface of these samples becomes much smoother and the amount of pores decreases, which can be attributed to an increase of the graphitization degree in NCNF-1000 samples. HRTEM images (Fig. S4, ESI†) also show that NCNF-1000 has more pronounced graphite layers than NCNF-800. The average diameter of NCNF-800 and NCNF-1000 fibers is 470 and 340 nm, respectively (Fig. S3b and e†). Shrinking of the nanofibers takes place at the

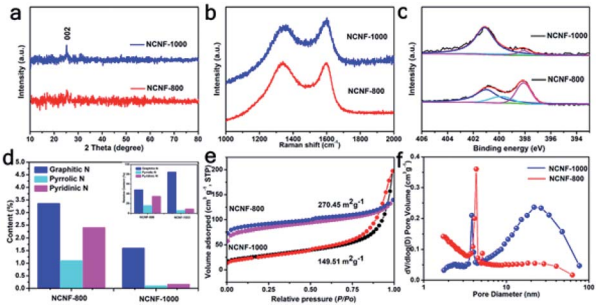

Fig. 2 Structure characterization of the porous NCNF-800 and NCNF-1000 samples. (a) XRD patterns. (b) Raman spectra. (c) High-resolution N 1s XPS spectra. (d) The corresponding contents of graphitic N, pyrrolic N and pyridinic N from (c). (e and f) BET and BJH curves.

higher temperatures, leading to a smaller diameter for the NCNF-1000 nanofibers.

The structural details of both samples were further investigated by XRD, Raman and X-ray photoelectron spectroscopy (XPS) as shown in Fig. 2. The XRD patterns of the NCNF-800 and NCNF-1000 samples show only one minor diffraction peak corresponding to the expanded graphite (002) lattice planes at about 26°. The peak becomes clearer and sharper for the NCNF-1000 sample. This confirms that the graphitization degree in the nanofibers is enhanced with increasing annealing temperature. Raman spectra exhibit two characteristic bands with a D band (approximately 1350 cm^{-1}) from disordered carbon and G band (~1600 cm^{-1}) from graphitic carbon (Fig. 2b). The areal intensity ratios of I_D/I_G, a factor to determine the graphitization degree, are calculated to be 2.68 and 2.41 for the NCNF-800 and NCNF-1000 samples, respectively (Table S1, ESI†). This confirms once more that the graphitization degree of NCNF-1000 is higher than that of NCNF-800. In addition, a quantitative measurement for the size of the sp^2-domains (L_a) can be given by applying the I_D/I_G ratio in the Tuinstra–Koenig relation.[29,30] The average size of sp^2-domains for these two samples is calculated to be 14.4 and 16.0 nm, respectively. An elemental analysis of the two NCNFs shows that the nitrogen content of NCNF-800 and NCNF-1000 is around 6.9 and 1.9 wt%, respectively (Table S2, ESI†). Clearly the relative nitrogen content rapidly decreases upon increasing the heat treatment temperature. XPS measurements were employed to analyze the nitrogen species, namely graphitic N, pyridinic N and pyrrolic N, in the two NCNF samples (Fig. 2c). The content of all of the N species decreases when the annealing temperature increases. Moreover, the loss of both pyridinic N and pyrrolic N in the NCNF-1000 sample is much more severe than that of the graphitic N (Fig. 2d). This is because graphitic N in the carbon framework is more stable than pyridinic N and pyrrolic N under high-temperature annealing. The surface and pore distribution in the two samples were also analyzed. On the basis of nitrogen adsorption–desorption analysis, the specific surface areas of the NCNF-800 and NCNF-1000 samples are 270.45 and 149.91 $m^2 g^{-1}$, respectively (Fig. 2e). The hysteresis loop of the NCNF-1000 sample at high pressure ($P/P_0 = 0.5$–1.0) reflects the presence of obvious mesopores. The pore distribution of NCNF-800 and NCNF-1000 shows that the NCNF-800 sample has more micropores than NCNF-1000, which is closely related to the structural defects in the nanofibers (Fig. 2f). This difference is mainly attributed to the different nitrogen doping concentrations in the NCNF-800 and NCNF-1000 samples.

Electrochemical performances in a PIB

The electrochemical performance of a half-cell potassium-ion battery using the as-prepared NCNF-800 and NCNF-1000 samples as freestanding binder-free anodes was measured to investigate the role of the nitrogen species (Fig. 3). First, cyclic voltammograms (CVs) of the NCNF-800 and NCNF-1000 were measured in the potential range from 0.01 to 3.0 V *vs.* K^+/K at a scan rate of 0.2 mV s^{-1} (Fig. S5, ESI†). In the first cathodic scan of NCNF-800 and NCNF-1000, a broad peak located at 0.01–1 V can be observed, which is attributed to the formation of an SEI (Solid Electrolyte Interphase) layer.[31] The four subsequent CV curves mostly overlap, showing good reversibility. No obvious redox peaks appear in the four subsequent CV curves of NCNF-800 due to the small size of the sp^2-domains and the discontinuous structural nature with more defective surfaces and interfaces. However, a broad anodic peak at 0.5 V and a broad cathodic peak at 0.9 V can be observed in NCNF-1000, in which the capacity mainly originates from the intercalation of K-ions into the graphitic layers (0.01–1 V).[32] When tested at 0.1 A g^{-1}, NCNF-800 shows a higher initial discharge capacity (422 mA h g^{-1}) than NCNF-1000 (345 mA h g^{-1}), indicating that there are more active sites for potassium storage in NCNF-800

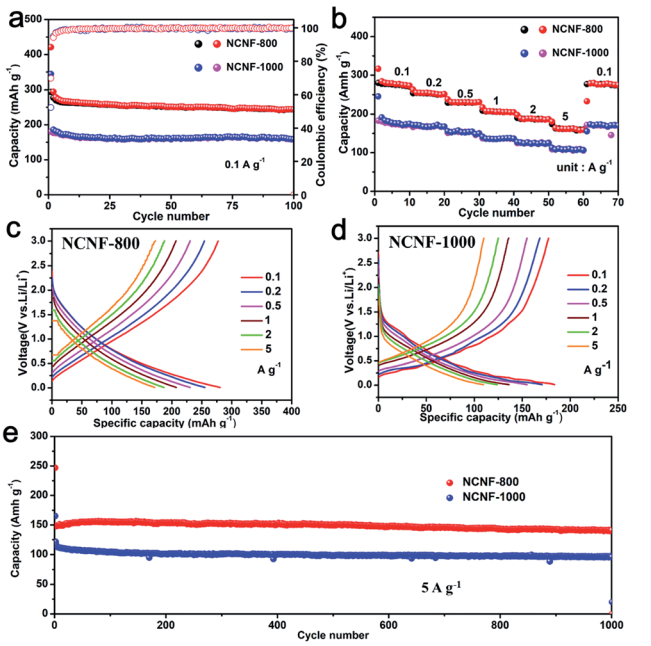

Fig. 3 Electrochemical properties of NCNF-800 and NCNF-1000. (a) Cycling performance of NCNF-800 and NCNF-1000 samples tested at a current density of 100 mA g^{-1}. (b) Rate performance of NCNF-800 and NCNF-1000 at various current densities from 0.1 to 5 A g^{-1}. (c and d) The corresponding charge and discharge voltage profiles of NCNF-800 and NCNF-1000 at different current densities. (e) Cycling performance of NCNF-800 and NCNF-1000.

(Fig. 3a). In NCNF-800, the capacity increase at the initial cycles may be attributed to a slowly increased electronic conductivity and an enhanced capability of ion-infiltration. The first-cycle coulombic efficiency of the NCNF-800 electrode is 69.7%, which is higher than that of NCNF-1000 (52.5%). The higher ICE of NCNF-800 (than that of NCNF-100) is mainly attributed to more reversible storage sites for K-ions, which is caused by higher nitrogen content. The rate performance was measured at different current densities ranging from 0.1 to 5 A g^{-1} (Fig. 3b). The average specific discharge capacities of NCNF-800 are 280, 260, 232, 210, 190 and 170 mA h g^{-1} at 0.1, 0.2, 0.5, 1, 2 and 5 mA h g^{-1}, respectively. However, for NCNF-1000 the corresponding specific discharge capacities are 180, 170, 157, 138, 126 and 112 mA h g^{-1}. When the current density returns to 0.1 A g^{-1}, the average specific discharge capacity of NCNF-800 recovers to 280 mA h g^{-1}, indicating an excellent rate performance. The corresponding charge and discharge voltage profiles of NCNF-800 and NCNF-1000 are shown in Fig. 3c and d, and S5.† It demonstrates that in NCNF-800, besides the extra capacity mainly occurring in the high potential window (from 1 to 2 V), the capacity in the low potential window (from 0.01 to 1 V) is also higher than that of NCNF-1000 (listed in Table S3, ESI†). In contrast, most of the capacity of NCNF-1000 is from the low energy window range of 0.01–1 V as shown in the CV curves (Fig. S5, ESI†). The capacity contributions from the high voltage (above 1 V) and low voltage (below 1 V) of the discharge can be calculated at different current densities, which are in agreement with the above-analysed results (Fig. S6, ESI†). The long-term cycling performances of NCNF-800 and NCNF-1000 were evaluated at a high current density of 5 A g^{-1} (Fig. 3e). NCNF-800 exhibits a higher specific capacity of 150 mA h g^{-1} after 1000 cycles than NCNF-1000, showing outstanding long-term cycling stability. Furthermore, electrochemical impedance spectroscopy (EIS) measurements were carried out to evaluate the charge-transfer resistance (R_{ct}) of the NCNF-800 sample at different cycles (Fig. S9, ESI†). The stable and small R_{ct} values of ~75 Ω at the 1st, 10th and 50th cycles indicate that the electronic mobility remains fast and stable during cycling. The contact resistance in PIBs is relatively low due to the good conductivity of the electrode materials and good contact between the electrode materials and electrolyte. The morphological changes after 1000 cycles were studied by SEM; it shows that the overall morphology of NCNF-800 remains the same (Fig. S10, ESI†). The electrochemical measurements clearly demonstrate that the NCNF-800 sample has extra capacity across the whole potential range and the extra capacity is reversible (*e.g.* stable in charge and discharge cycles).

In situ TEM and *ex situ* EELS study of electrochemical potassiation

To provide a more detailed insight into the potassiation process of the NCNF-800 and NCNF-1000 samples, *in situ* TEM was carried out to study the microstructural evolution in real time (Fig. 4 and 5).[33] Both TEM images and SAED patterns were recorded during potassiation. The results reveal the following main characteristics during the potassiation process: (1) both

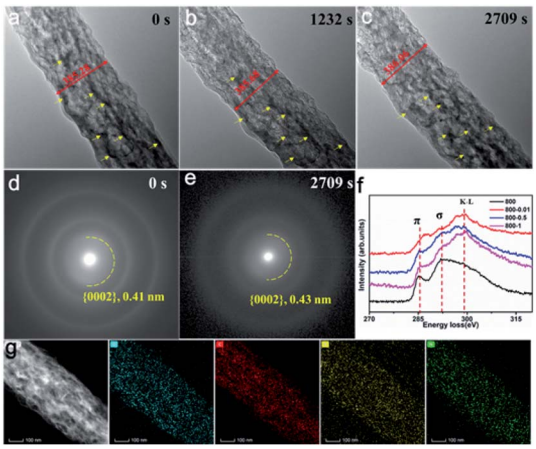

Fig. 4 Evolution of the morphology and microstructure of NCNF-800 during potassiation. A nanobattery was designed inside the TEM with NCNF-800 as the cathode, potassium metal as the anode, and K_2O grown on the surface of the potassium metal as the solid electrolyte. When a bias of −10 V is applied, a potassiation process is triggered. (a–c) The morphological evolution of NCNF-800 during the potassiation reaction. (d and e) Electron diffraction patterns of NCNF-800 before and after the potassiation reaction. (f) The *ex situ* C K-edge spectra from the edge region in different states. (g) STEM-HAADF image and the corresponding STEM-EDS maps of potassiated NCNF-800.

NCNF-800 and NCNF-1000 exhibit a negligible volume expansion during the K^+ insertion (Fig. 4a–c and 5a–c). The volume expansion is only about 0.5% of NCNF-800 (its diameter expands from 385.3 nm to 386.0 nm), similar to that of NCNF-1000 (its diameter expands from 507.8 nm to 508.7 nm). This is attributed to the

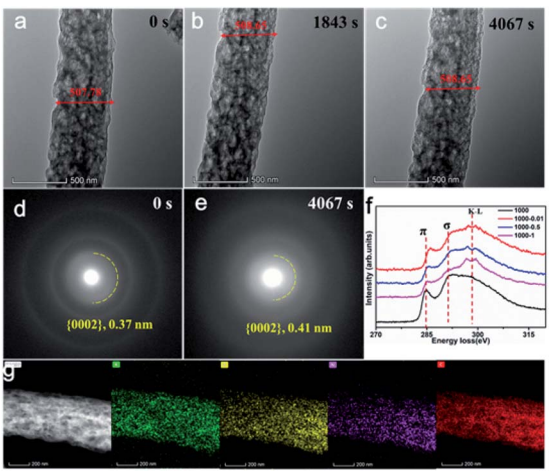

Fig. 5 Evolution of the morphology and microstructure of NCNF-1000 during potassiation. A nanobattery was designed inside the TEM with NCNF-1000 as the cathode, potassium metal as the anode, and K_2O grown on the surface of potassium metal as the solid electrolyte. When a bias of −10 V is applied, a potassiation process is triggered. (a–c) The morphological evolution of NCNF-1000 during the potassiation reaction. (d and e) Electron diffraction patterns of NCNF-1000 before and after the potassiation reaction. (f) The corresponding charge and discharge voltage profiles of NCNF-800 and NCNF-1000 at different current densities. (f) *Ex situ* C K-edge spectra from the edge region at different states. (g) STEM-HAADF image and the corresponding STEM-EDS maps of potassiated NCNF-1000.

porous structure of the NCNFs, which can efficiently accommodate the volume changes and maintain structural stability during potassiation. (2) Although the overall volume expansion is quite small, the image contrast in both samples changes slightly and becomes grainy upon potassiation, as marked by the yellow arrowheads in Fig. 4a–c and S11d–f.† The varying image contrast implies the local volumetric expansion due to insertion of K. (3) The phase transformation from C to KC_x due to K-intercalation is identified in both samples by dynamic SAED patterns. Before potassiation, as identified by the rings in the SAED patterns, the {002} plane spacings of pristine NCNF-800 and NCNF-1000 are 4.1 Å and 3.7 Å, respectively. These spacings are slightly larger than the one of perfect graphite (3.6 Å) due to the disordered structure in NCNFs (Fig. 4d). As the pristine NCNF-800 is more defective with a lower graphitization degree, its {002} lattice plane spacing is larger than that of the NCNF-1000. After complete potassiation, the {002} plane spacing of potassiated NCNF-800 increases from 4.1 to 4.3 Å, corresponding to an increment rate of around 5%. For NCNF-1000, the {002} spacing increases from 3.7 to 4.1 Å, corresponding to an increment rate of about 11%. Although the increment rates are different, the final products (*e.g.* KC_x) are the same, implying that there is a similar K-ion intercalation process. Therefore, while the capacity of the highly graphitized NCNF-1000 mainly originates from an intercalation reaction, additional potassium storage capacity is also from the abundant nanopores and N-related defects in NCNF-800. (4) K has been identified by energy-dispersive X-ray spectroscopy (EDS) mapping, which shows that K is uniformly distributed on both the potassiated NCNF-800 and NCNF-1000 samples (Fig. 4g and 5g).

The charge states of C and K in the NCNF-800 and NCNF-1000 samples were investigated in the pristine state as well as after the first cycle when discharged at different potentials by electron energy loss spectroscopy (EELS) as shown in Fig. 4f and 5f, to uncover their reaction mechanism. All EELS spectra were calibrated with respect to the zero-loss peak. The pristine NCNF-800 has two typical C-K edges, *i.e.* the π*-edge at 285.3 eV and the σ*-edge at 291.8 eV (Fig. 4f). The positions of these two edges are slightly shifted to a higher energy compared to those of perfect graphite (π*-edge near 284.5 eV and σ*-edge near 290 eV).[34,35] This is because the conduction band of C-atoms at defective sites has a higher energy than that of perfect graphite (so the graphitic carbons have a slightly higher valence state than that of perfect graphite). When the PIB with NCNF-800 as the anode is discharged to 1 V and beyond, the K-L edge is observed at 296 eV, confirming the insertion of K^+ into the NCNF-800 sample. When the PIB with NCNF-800 as the anode is discharged to 1 V and even to 0.5 V, the π*-edge position of the C-K edge shows no obvious shift, showing that at this stage the majority of the 2D graphitic C-atoms are still not the major host for storing K^+. When further discharged to 0.01 V, the π*-peak shifts to a higher energy (287.4 eV) compared with that of the pristine NCNF-800, implying a local electron transfer from K ions to the C planar π bonds. This shift can be attributed to the formation of C-K bonds, implying that the intercalation reaction becomes dominant when the voltage of discharge is below 0.5 V. As for the σ*-edge (which represents the energy difference between a carbon K-shell and the σ*-conducting bond), the position shifts from 291.8 eV for the pristine NCNF-800 sample to 292.0 eV for the 1 V-discharged sample, 292.1 eV for the 0.5 V-discharged sample and 291.4 eV for the 0.01 V-discharged sample. The shift to high energy may be caused by the formation of 3D dangling bonds between C and the adatoms such as K.

As for the pristine NCNF-1000 sample, there are two typical C-K edges located at 284.8 eV (π*-peak) and 291.8 eV (σ*-peak) in the EELS spectrum as shown in Fig. 5f. The π*-peak position is lower than that of the pristine NCNF-800 and closer to that in the perfect graphite crystal, which may be due to the lower nitrogen content and fewer C–N bonds formed in NCNF-1000. When discharged to 1 V, there is a K-L edge located near 294 eV, implying the presence of K-ions in the structure. The C π*-peak gradually shifts from 285.1 eV to 285.6 eV, and finally to 286 eV, upon discharging. The continuous shift indicates that insertion of K^+ directly modifies the planar framework of the π bonds as well. As for the σ*-peak, the position undergoes no obvious shift when discharged to 1 V and even to 0.5 V. However, when discharging to 0.01 V, it shifts to 292.6 eV.

The EELS studies reveal the different behaviors of the C near edge peaks upon discharging. When the discharging voltage is higher than 0.5 V, the overall σ*-peak of the NCNF-800 sample is higher than that of NCNF-1000, an indication of more active sites on the surface and interfaces in the N-rich NCNF-800 sample. At a discharging voltage of 0.01 V, the N-rich NCNF-800 sample shows a relatively higher local electron transfer into the C planar π bonds, because of the presence of K ions (287.4 eV), than the NCNF-1000 sample (286.0 eV), implying that the graphitic carbon is participating more deeply in the storage of K-ions. Meanwhile, at a discharging voltage of 0.01 V, the σ*-peak of the N-rich NCNF-800 sample (291.4 eV) is lower than that of the NCNF-1000 sample (292.6 eV), implying an easy diffusion of the tangled adatoms enabling the deep intercalation reaction.

As measured in the Raman spectra of NCNF-800 (Fig. S12a†), the I_D/I_G ratio decreased from 0.97 to 0.94 when the sample was discharged from 1 to 0.01 V, showing an increased degree of graphitization. This phenomenon may be attributed to the absorption of K^+ into nitrogen-induced defects during the potassiation process, thus reducing the degree of disorder of NCNF-800.[41] However, the I_D/I_G values of NCNF-1000 increased from 0.94 to 1.06 when the sample was discharged from 1 V to 0.01 V (Fig. S12b†). This is due to the intercalation of K^+ into graphitic layers during potassiation and thus the decrease of the graphitization degree.[36] Therefore, combined with *in situ* TEM and *ex situ* EELS, the above Raman results demonstrate that N-doping in carbon materials plays an important role in their potassium storage mechanism.

Theoretical calculations on potassium storage

To further reveal the active/storage sites in the NCNFs for PIBs, a series of DFT simulations were carried out (Fig. 6).[37–39] The structure of the NCNF samples was modeled, consisting of small N-doped graphene layers with atomic vacancies. The

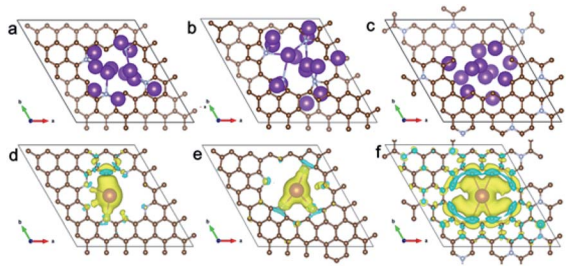

Fig. 6 Effects of N species studied by DFT calculations. (a–c) Calculated models for K storage based on pyridinic N-Gr, pyrrolic N-Gr and graphitic N-Gr sheets with a hole containing four N atoms. (d–f) Variation of the average adsorption energy along with K atom numbers for different N-doped graphenes. Brown, gray, and purple balls represent C, N, and K atoms, respectively. Yellow and blue areas represent the increased and decreased electron density, respectively.

doped N was modelled as three different kinds of species: pyridinic, pyrrolic and graphitic N. While the pyridinic and pyrrolic N are located on the edges, the vacancies or on the surface, the graphitic N can locate inside the small 2D graphite lattice.[40] The average energy of K-ion insertion, either as an adatom attached to the vacancies/defects (either on the surface or in the interfaces) or as an intercalated ion among the graphitic layers, has been calculated. Typically, four dopant N atoms are added around atomic vacancies to perform a qualitative calculation to reveal the effect of the different nitrogen species. We assume that no further K-ions will be inserted when the average K-ion adsorption energy exceeds 0 eV. The calculated results show that the graphitic N-Gr, pyridinic N-Gr and pyrrolic N-Gr can store 12, 12, and 14 K-ions, respectively, in the nearby vacancies (Fig. 6a–c and S13, ESI†). Because of the nature of pyridinic N and pyrrolic N, they can form bonds directly with the inserted K-ions, affording more atomic vacancies around them (compared to graphitic N). Furthermore, electron density difference maps were calculated to investigate the effect of different N species on their bonding structure with the adsorbed K atoms (Fig. 6d–f). When one K atom is introduced into a structure with pyridinic N and pyrrolic N, the charge density of the adsorbed K atom is mainly concentrated around the pyridinic N and pyrrolic N sites. However, for the graphitic N model, the introduced K atom preferentially interacts with several nearby carbon atoms rather than with a single graphitic N. Therefore, pyridinic N and pyrrolic N display a stronger K adsorption ability than graphitic N.[41] This explains the extra capacity of the N-doped samples in the high voltage range, mainly through chemical absorption by forming a direct bond between the N and K ions. Such an effect occurs mainly on surfaces and interfaces.

Graphitic N is a little more negative than its surrounding C and will therefore cause intercalation of the K-ion by sharing bonds with its surrounding C. Such a process will enlarge the spacing of the local graphitic layers and lower the diffusion energy of the K-ions, which will promote a quick and full intercalation during discharge. This explains why the N-doped sample also has a large capacity in the low-energy window when the intercalation reaction dominates.

Discussion on the origin of the extra capacity

The extra capacity of the N-doped nanofibers has two origins: (1) chemical absorption due to the pyridinic N and pyrrolic N induced atomic vacancies/surfaces; (2) extra intercalation capacity because of the graphitic N. In the sample with high N content, K tends to directly form bonds with pyridinic N and pyrrolic N and be absorbed as K–N–C clusters when discharged at high potential. At low potential when the intercalation reaction becomes the major K storage mechanism, the graphitic N serves as the preferential site for K-intercalation to prompt a full and deep K-intercalation. Thus there is also the extra capacity created when charged at the low potential. Practically, the improved potassium storage properties of the N-doped NCNF-800 are also attributed to the microporous structure. The porous architecture generates a high BET specific surface area, which can provide more reaction active/storage sites and so enhance the electrode/electrolyte contact area. Additionally, interior interconnected voids and/or abundant micropores can efficiently facilitate mass transport, and hence guarantee a continuous electron transport and accommodate volume variations and strain during the potassiation/depotassiation process. As doped N will normally introduce defects into the carbon matrix, the morphology of the surface and size of pores will be influenced by the N-content. Meanwhile, the doped N enhances the K^+-ion surface absorption and increases the capacity, making it difficult to clearly separate the capacity contribution from surface and N-species in the two samples. However, the N-content has the major effect on the surface/pore morphology, the mechanism of K-ion storage, and thus also the increased capacity.

Conclusions

The origin of the extra capacity of PIBs in the N-doped nanofiber anode has been revealed. Besides the capacity related to the chemical absorption in the high potential window (>1 V), an extra capacity is created by the enhanced intercalation process in the low potential window (0.01–1 V). The chemical absorption is mainly caused by the pyridinic N and pyrrolic N in the defective sites, while the intercalation reaction is enhanced by the graphitic N which attracts K-ions and lowers the ion diffusion energy. In addition, the resultant NCNF samples possess a high surface area, tunable nitrogen species and abundant interconnected nanopores, which are favorable for potassium storage. NCNF-800 samples as PIB anodes deliver a higher reversible capacity of 290 mA h g^{-1} at 100 mA g^{-1} than NCNF-1000 samples (180 mA h g^{-1}). The present work provides a reasonable direction for a rational design and deep understanding of functional nitrogen-doped carbon materials toward energy-related applications.

Conflicts of interest

There are no conflicts to declare.

Acknowledgements

F. Liu and J. S. Meng contributed equally to this work. This work was supported by the National Natural Science Foundation of

China (51832004 and 51521001), the National Key Research and Development Program of China (2016YFA0202603), and the Natural Science Foundation of Hubei Province (2019CFA001). The S/TEM work was performed at the Nanostructure Research Center (NRC), which is supported by the Fundamental Research Funds for the Central Universities (WUT: 2019III012GX, 2020III002GX), the State Key Laboratory of Advanced Technology for Materials Synthesis and Processing, and the State Key Laboratory of Silicate Materials for Architectures (all of the laboratories are at Wuhan University of Technology).

References

1 S. Chu, Y. Cui and N. Liu, *Nat. Mater.*, 2016, **16**, 16–22.
2 V. R. Stamenkovic, D. Strmcnik, P. P. Lopes and N. M. Markovic, *Nat. Mater.*, 2016, **16**, 57–69.
3 J. Meng, H. Guo, C. Niu, Y. Zhao, L. Xu, Q. Li and L. Mai, *Joule*, 2017, **1**, 522–547.
4 F. Cheng, J. Liang, Z. Tao and J. Chen, *Adv. Mater.*, 2011, **23**, 1695–1715.
5 Y. Tang, Y. Zhang, W. Li, B. Ma and X. Chen, *Chem. Soc. Rev.*, 2015, **44**, 5926–5940.
6 J. C. Pramudita, D. Sehrawat, D. Goonetilleke and N. Sharma, *Adv. Energy Mater.*, 2017, **7**, 1602911.
7 K. Chayambuka, G. Mulder, D. L. Danilov and P. H. L. Notten, *Adv. Energy Mater.*, 2018, **8**, 1800079.
8 L. Fan, R. Ma, Q. Zhang, X. Jia and B. Lu, *Angew. Chem., Int. Ed.*, 2019, **58**, 10500–10505.
9 X. Wu, Y. Chen, Z. Xing, C. W. K. Lam, S. S. Pang, W. Zhang and Z. Ju, *Adv. Energy Mater.*, 2019, **9**, 1900343.
10 X. Liu and L. Dai, *Nat. Rev. Mater.*, 2016, **1**, 16064.
11 L.-F. Chen, Y. Lu, L. Yu and X. W. Lou, *Energy Environ. Sci.*, 2017, **10**, 1777–1783.
12 H. X. Zhong, J. Wang, Y. W. Zhang, W. L. Xu, W. Xing, D. Xu, Y. F. Zhang and X. B. Zhang, *Angew. Chem., Int. Ed.*, 2014, **53**, 14235–14239.
13 J. Meng, C. Niu, L. Xu, J. Li, X. Liu, X. Wang, Y. Wu, X. Xu, W. Chen, Q. Li, Z. Zhu, D. Zhao and L. Mai, *J. Am. Chem. Soc.*, 2017, **139**, 8212–8221.
14 C. Niu, J. Meng, X. Wang, C. Han, M. Yan, K. Zhao, X. Xu, W. Ren, Y. Zhao, L. Xu, Q. Zhang, D. Zhao and L. Mai, *Nat. Commun.*, 2015, **6**, 7402–7410.
15 Q. Lai, Y. Zhao, Y. Liang, J. He and J. Chen, *Adv. Funct. Mater.*, 2016, **26**, 8334–8344.
16 W. Wang, J. Zhou, Z. Wang, L. Zhao, P. Li, Y. Yang, C. Yang, H. Huang and S. Guo, *Adv. Energy Mater.*, 2018, **8**, 1701648.
17 B. Cao, Q. Zhang, H. Liu, B. Xu, S. Zhang, T. Zhou, J. Mao, W. K. Pang, Z. Guo, A. Li, J. Zhou, X. Chen and H. Song, *Adv. Energy Mater.*, 2018, **8**, 1801149.
18 M. Yang and Z. Zhou, *Adv. Sci.*, 2017, **4**, 1600408.
19 H. Cui, Z. Zhou and D. Jia, *Mater. Horiz.*, 2017, **4**, 7–19.
20 L. Dai, Y. Xue, L. Qu, H. J. Choi and J. B. Baek, *Chem. Rev.*, 2015, **115**, 4823–4892.
21 Y. Ito, Y. Shen, D. Hojo, Y. Itagaki, T. Fujita, L. Chen, T. Aida, Z. Tang, T. Adschiri and M. Chen, *Adv. Mater.*, 2016, **28**, 10644–10651.
22 X. Kong, Q. Liu, D. Chen and G. Chen, *ChemCatChem*, 2017, **9**, 846–852.
23 K. Share, A. P. Cohn, R. Carter, B. Rogers and C. L. Pint, *ACS Nano*, 2016, **10**, 9738–9744.
24 Y. Xu, C. Zhang, M. Zhou, Q. Fu, C. Zhao, M. Wu and Y. Lei, *Nat. Commun.*, 2018, **9**, 1720–1730.
25 Y. Liu, N. Zhang, C. Yu, L. Jiao and J. Chen, *Nano Lett.*, 2016, **16**, 3321–3328.
26 Q. Liu, Y. Wang, L. Dai and J. Yao, *Adv. Mater.*, 2016, **28**, 3000–3006.
27 L. Li, Z. Wu, S. Yuan and X.-B. Zhang, *Energy Environ. Sci.*, 2014, **7**, 2101–2122.
28 W. Feng, Y. Cui, W. Liu, H. Wang, Y. Zhang, Y. Du, S. Liu, H. Wang, X. Gao and T. Wang, *ACS Nano*, 2020, **14**, 4938–4949.
29 V. López, R. S. Sundaram, C. Gómez-Navarro, D. Olea, M. Burghard, J. Gómez-Herrero, F. Zamora and K. Kern, *Adv. Mater.*, 2009, **21**, 4683–4686.
30 F. Tuinstra and J. L. Koenig, *J. Chem. Phys.*, 1970, **53**, 1126–1130.
31 W. Zhang, J. Ming, W. Zhao, X. Dong, M. N. Hedhili, P. M. F. J. Costa and H. N. Alshareef, *Adv. Funct. Mater.*, 2019, **29**, 1903641.
32 Z. Zhang, B. Jia, L. Liu, Y. Zhao, H. Wu, M. Qin, K. Han, W. A. Wang, K. Xi, L. Zhang, G. Qi, X. Qu and R. V. Kumar, *ACS Nano*, 2019, **13**, 11363–11371.
33 J. Y. Huang, L. Zhong, C. M. Wang, J. P. Sullivan, W. Xu, L. Q. Zhang, S. X. Mao, N. S. Hudak, X. H. Liu and A. Subramanian, *Science*, 2010, **330**, 1515–1520.
34 D. M. Haiber and P. A. Crozier, *ACS Nano*, 2018, **12**, 5463–5472.
35 R. J. Nicholls, A. T. Murdock, J. Tsang, J. Britton, T. J. Pennycook, A. Koós, P. D. Nellist, N. Grobert and J. R. Yates, *ACS Nano*, 2013, **7**, 7145–7150.
36 R. Guo, X. Liu, B. Wen, F. Liu, J. Meng, P. Wu, J. Wu, Q. Li and L. Mai, *Nano-Micro Lett.*, 2020, **12**, 148.
37 Y. Liu, H. Dai, L. Wu, W. Zhou, L. He, W. Wang, W. Yan, Q. Huang, L. Fu and Y. Wu, *Adv. Energy Mater.*, 2019, **9**, 1901379.
38 H. Wang, G. Yang, Z. Chen, J. Liu, X. Fan, P. Liang, Y. Huang, J. Lin and Z. Shen, *J. Power Sources*, 2019, **419**, 82–90.
39 J. Liu, T. Yin, B. Tian, B. Zhang, C. Qian, Z. Wang, L. Zhang, P. Liang, Z. Chen, J. Yan, X. Fan, J. Lin, X. Chen, Y. Huang, K. Loh and Z. Shen, *Adv. Energy Mater.*, 2019, **9**, 1900579.
40 R. Arenal, K. March, C. P. Ewels, X. Rocquefelte, M. Kociak, A. Loiseau and O. Stéphan, *Nano Lett.*, 2014, **14**, 5509–5516.
41 W. Yang, J. Zhou, S. Wang, W. Zhang, Z. Wang, F. Lv, K. Wang, Q. Sun and S. Guo, *Energy Environ. Sci.*, 2019, **12**, 1605–1612.

